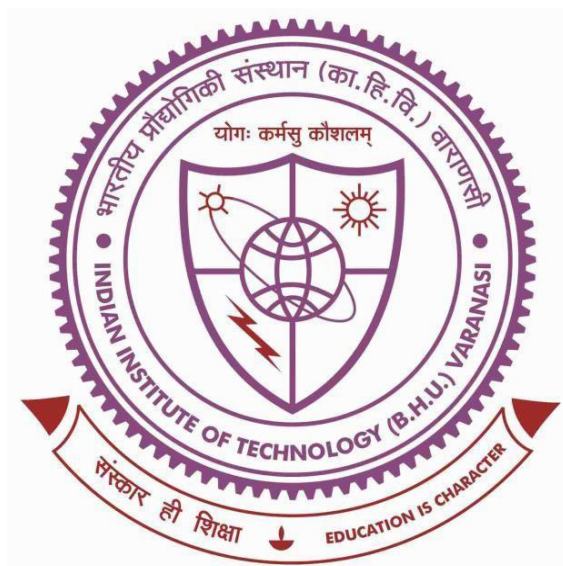


Design and Characterization of Ultrafine-Grained Ferritic and Nanostructured Bainitic Steels Processed by Electropulsing Technique



Thesis submitted in partial fulfilment for the
Award of Degree

Doctor of Philosophy

by

Debabrata Bhuyan

DEPARTMENT OF METALLURGICAL ENGINEERING
INDIAN INSTITUTE OF TECHNOLOGY
(BANARAS HINDU UNIVERSITY)
VARANASI-221005, INDIA

17141002

2023

CERTIFICATE

It is certified that the work contained in the thesis titled "*Design and Characterization of Ultrafine-Grained Ferritic and Nanostructured Bainitic Steels Processed by Electropulsing Technique*" by *Debabrata Bhuyan* has been carried out under our supervision and this work has not been submitted elsewhere for a degree.

It is further certified that the student has fulfilled all the requirements of Comprehensive, Candidacy and SOTA for the award of Ph.D. degree.



Dr. Rampada Manna

(Supervisor) 11/08/2023

Department of Metallurgical Engineering
Indian Institute of Technology
(Banaras Hindu University)
Varanasi-221005, India

सह-आचार्य

Associate Professor

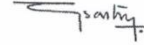
धातुकीय अभियांत्रिकी विभाग

Department of Metallurgical Engg.

भारतीय प्रौद्योगिकी संस्थान (काशी हिन्दू विश्वविद्यालय)

Indian Institute of Technology (Banaras Hindu University)

वाराणसी-२२१००५/Varanasi-221005



Prof. G.V.S Sastry

(Co-Supervisor)

Department of Metallurgical Engineering
Indian Institute of Technology
(Banaras Hindu University)
Varanasi-221005, India

Varanasi-221005, India

धातुकीय अभियांत्रिकी विभाग

Department of Metallurgical Engg.

भारतीय प्रौद्योगिकी संस्थान (काशी हिन्दू विश्वविद्यालय)

Indian Institute of Technology (Banaras Hindu University)

वाराणसी-221005/Varanasi-221005

DECLARATION BY THE CANDIDATE

I, **Debabrata Bhuyan**, certify that the work embodied in this thesis is my own bonafide work and carried out by me under the supervision of **Dr. Rampada Manna** and **Prof. G.V.S Sastry** from **July 2017** to **August 2023**, at the **Department of Metallurgical Engineering**, Indian Institute of Technology (BHU), Varanasi. The matter embodied in this thesis has not been submitted for the award of any other degree/diploma. I declare that I have faithfully acknowledged and given credits to the research workers wherever their works have been cited in my work in this thesis. I further declare that I have not willfully copied any other's work, paragraphs, text, data, results, *etc.*, reported in journals, books, magazines, reports dissertations, theses, *etc.*, or available at websites and have not included them in this thesis and have not cited as my own work.




Debabrata Bhuyan

Date: 11-8-2023

CERTIFICATE BY THE SUPERVISORS

It is certified that the above statement made by the student is correct to the best of our knowledge.


Dr. Rampada Manna
(Supervisor) 11/08/2023

Department of Metallurgical Engineering
Indian Institute of Technology
(Banaras Hindu University)
Varanasi-221005, India
Associate Professor
धातुकीय अभियांत्रिकी विभाग
Department of Metallurgical Engg.
भारतीय प्रौद्योगिकी संस्थान (काशी हिन्दू विश्वविद्यालय)
Indian Institute of Technology (Banaras Hindu University)
वाराणसी-221005/Varanasi-221005


Prof. G.V.S Sastry
(Co-Supervisor)

Department of Metallurgical Engineering
Indian Institute of Technology
(Banaras Hindu University)
Varanasi-221005, India
Professor
धातुकीय अभियांत्रिकी विभाग
Department of Metallurgical Engg.
भारतीय प्रौद्योगिकी संस्थान (काशी हिन्दू विश्वविद्यालय)
Indian Institute of Technology (Banaras Hindu University)
वाराणसी-221005/Varanasi-221005


Prof. Sunil Mohan
(Head of the Department)

Department of Metallurgical Engineering
Indian Institute of Technology
(Banaras Hindu University)
Varanasi-221005, India
विभागाध्यक्ष / HEAD
धातुकीय अभियांत्रिकी विभाग
Department of Metallurgical Engg.
भारतीय प्रौद्योगिकी संस्थान (काशी हिन्दू विश्वविद्यालय)
Indian Institute of Technology (Banaras Hindu University)
वाराणसी-221005/Varanasi-221005

COPYRIGHT TRANSFER CERTIFICATE

Title of the Thesis:

“Design and Characterization of Ultrafine-Grained Ferritic and Nanostructured Bainitic Steels Processed by Electropulsing Technique”

Name of the Student: Mr. Debabrata Bhuyan

COPYRIGHT TRANSFER

The undersigned hereby assigns to the Indian Institute of Technology (Banaras Hindu University) Varanasi all rights under copyright that may exist in and for the above thesis submitted for the award of the *Ph.D. Degree*.

Date: 11/8/2023

Debabrata Bhuyan
Debabrata Bhuyan

Note: However, the author may reproduce or authorize others to reproduce material extracted verbatim from the thesis or derivative of the thesis for author's personal use provided that the source and the Institute's copyright notice are indicated.

ACKNOWLEDGEMENTS

I am very grateful and indebted to my supervisors **Dr. Rampada Manna and Prof. G.V.S Sastry** for their consistent help, encouragement, valuable discussions, and also the faith in me during the entire period of my research work. I would not have been able to complete the thesis without their utmost involvement and invaluable efforts. They motivated me to pursue research problems and the need for persistent effort to accomplish the goal.

I would like to thank RPEC committee members: Dr. Joysurya Basu and Dr. Mohd Zaheer Khan Yusufzai for their insightful comments and encouragement.

I am highly thankful Prof. Sunil Mohan Head of the Department and former Heads Prof. N. K. Mukhopadhyay and Prof. R.K. Mandal for their support.

My special thanks go to Prof. Vakil Singh, Emeritus Faculty, Department of Metallurgical Engineering IIT (BHU), who taught me a lot to convert the present work into the shape of thesis. I am also thankful to Prof. N. C. Santhi Srinivas, Prof. B.N. Sharma, Prof. O.P. Sinha, Dr. K. Chattopadhyay, Dr. C.K. Behera, Dr. N. K Prasad, Dr. Sudipta Patra, Dr. S. D. Yadav and all the faculty members for their valuable suggestion as well as teaching during course work.

I would like to thank Prof. S.N Ojha and Prof R.K. Pandey for their suggestions related to electropulsing and Dr. Archana sharma, Dr. Surrender Sharama, Hitesh Choudhury and Sukanta Mishra from BARC, Vishakhapatnam for helping in electropulsing experiment and giving valuable suggestions.

My sincere thanks to Dr. Sumanta kumar Pradhan, Dr. Bhupeswar Mahato and Mr. Manoranjan Jena from NML Jamshedpur for giving me access to the facilities and helping me in conducting characterization.

I would like to acknowledge the Advanced Research Centre for Iron and Steel of the institute, funded by Ministry of Steel, Government of India, for Induction Melting Furnace and X-ray diffractometer Facility

I would like to thank to CIFC, IIT (BHU) for providing various facilities for the analysis.

I would also like to thank Professor I. Samajdar, Indian Institute of Technology Bombay, for extending the OIM facility.

I am also thankful to all Lab staffs (Lalit Singh, Anjani Singh, Ramashray Yadav) and all office staffs of the department.

The unforgettable moments, idea sharing, anytime support, appraisal, inspiration given by all my seniors (Dr. Deepa Verma, Dr. Rajbahadur Singh, Dr. Yagnesh Shadangi, Aman lal Das), batch mates (Dr. Sharvan Kumar, Roopchand, Sandeep, Jaydeep, Dr. M.D. Rao...), and juniors (Pavan, Amit, Manish, Priyatosh...) are the strength of mine that supported me in all endeavors.

Last but not the least, I would like to thank my family for supporting me.



Debabrata Bhuyan

Table of Content

	Page No.
ACKNOWLEDGEMENTS	iv
Table of Content	vi
List of Figures	xi
List of Tables	xviii
List of Symbols	xx
Abbreviations	xxii
Preface	xxiv
Chapter 1: Introduction and Literature survey	1
1.1 Introduction	2
1.2 Equal-channel angular pressing	3
1.2.1 The strain imposed in ECAP	4
1.2.2 The fundamental processing routes in ECAP	5
1.2.3 Strain development in different processing routes	6
1.2.4 Microstructure and mechanical properties of ECAPed material	7
1.3 Electropulsing	11
1.3.1 Electroplasticity	12
1.3.2 Accelerated recrystallization	14
1.3.3 Nanocrystallization	15
1.3.4 Theories on Electropulsing	17
1.4 Transformations in steel	18

1.5 Bainitic transformation	19
1.5.1 Theories related to bainitic transformation.....	19
1.5.2 Cementite precipitation in bainite.....	21
1.5.3 Carbide-free bainite	22
1.5.4 Nanostructured bainitic steel	24
1.5.5 Orientation relationship and variant pairing.....	25
1.5.6 Stability of the retained austenite	28
1.5.7 Tensile properties of nanostructured bainite	31
1.5.8 Work hardening behaviour	33
1.5.9 The incomplete-reaction phenomenon (T_0 and T_0' Concept).....	34
1.5.10 Acceleration of bainitic Transformation.....	36
1.6 Acceleration of phase transformation by electropulsing	37
1.6.1 Thermodynamic effects	37
1.6.2 Kinetic effects.....	39
1.7 Motivation	40
1.8 Objectives of the present investigation	41
Chapter 2: Materials and methods	42
2.1 Introduction	43
2.2 Effect of alloying elements	43
2.3 Materials selection and design	45
2.4 ECAP of D1 sample	47

2.5 Making of alloy D2	48
2.6 Heat treatment	49
2.7 Electropulsing	50
2.8 Microstructural characterization	52
2.8.1 Optical and scanning electron microscopy	52
2.8.2 X-ray diffraction	52
2.8.3 Transmission electron microscopy	55
2.8.4 Electron back scattered diffraction	56
2.9 Mechanical properties	56
Chapter 3: Structure and mechanical properties of UFG low carbon steel processed by ECAP followed by electropulsing	59
3.1 Introduction	60
3.2 Results	60
3.2.1 ECAP of D1 sample	60
3.2.2 Electropulsing of ECAP-6 sample.....	61
3.3 Discussion	72
3.3.1 Contribution of Joule heating towards grain modification	73
3.3.2 Athermal effect of electropulsing	74
3.3.3 Effect of skin depth.....	76
3.3.4 Grain modification mechanism	77
3.3.5 Mechanical properties.....	77
3.4 Conclusions	79

Chapter 4: Microstructure of bulk nanostructured steel	80
4.1 Introduction	81
4.2 Results	81
4.3 Discussion	94
4.3.1 Effect of alloy content and austempering time on the volume fraction of bainite ..	94
4.3.2 Effect of austempering time on microstructure	97
4.3.3 Effect of dislocation density on plate and sheaf thickness of bainite	99
4.3.4 Effect of austempering time on crystallographic variant selection	102
4.4 Conclusions	104
Chapter 5: Strengthening and hardening behaviour of nanostructured bainitic steel	106
5.1 Introduction	107
5.2. Results	107
5.3. Discussion	114
5.3.1 Distribution of carbon and dislocations in RA	114
5.3.2 Major factors contributing yield strength	115
5.3.3 Effect of carbon distribution in RA on work hardening behaviour	116
5.3.4 Work hardening mechanism	118
5.4 Conclusions	120
Chapter 6: Effect of electropulsing on stability of retained austenite and nanostructured bainite	121
6.1. Introduction	122
6.2. Results	122

6.3. Discussion	136
6.3.1 Thermal effect of electropulsing.....	137
6.3.2 Athermal effect of electropulsing	140
6.3.3 Carbide precipitation and dissolution	140
6.3.4 Electropulsing assisted bainite and martensite formation	142
6.4. Conclusions	145
Chapter 7: Effect of electropulsing on martensite	146
7.1 Introduction	147
7.2 Results	147
7.3 Discussion	158
7.3.1 Stability of martensite.....	158
7.3.2 Transformations in retained austenite.....	160
7.3.3 Changes in hardness after electropulsing	161
7.4 Conclusions	162
Chapter 8: Summary and Suggestions for Future Work	163
8.1 Conclusions of the present work	164
8.2 Suggestions for future work	165
References	167

List of Figures

	Page No.
Figure 1.1. ECAP die assembly with intersection angles of φ and ψ along with reference directions [14].	4
Figure 1.2. Schematic diagrams showing fundamental processing routes of ECAP [16].	5
Figure 1.3. Schematic diagram showing strain development with each pass of ECAP using processing routes A, B _A , B _C and C [18]	6
Figure 1.4. Different steels showing Hall–Petch relationship [25]. (Open symbols are for SPD materials, ‘ATP’ represents advanced thermomechanical processing and ‘Conv’ stands for conventional).	9
Figure 1.5. Variation in ductility with grain size for bcc steels. Open and filled symbols represent total elongation and uniform elongation in tension respectively [25].	10
Figure 1.6. (a) Engineering stress–strain plots for pure Cu. (Plot A is annealed, coarse grained Cu; B is 95% cold worked (CW) at room temperature; C is 93% CW at liquid-nitrogen temperature; D is 93% CW +180° C for 3 min.; and E, 93% CW +200° C, 3 min (b) TEM BF image of condition E showing bimodal grain distribution [28].	11
Figure 1.7. Load vs. extension plot of a zinc single crystal at 78K during the application of a DC pulse (100V – 1.5 x 10 ⁵ A/cm ²)	13
Figure 1.8. Ti-7Al subjected to 2% of plastic strain at room temperature (a) without pulsing and (b) after pulsing [32].	14
Figure 1.9. Optical micrographs of a cold worked brass after annealing at (a) 570 ⁰ C, (b) 650 ⁰ C and (c) after electropulsing treatment [46].	15
Figure 1.10. SEM micrographs (a) Austenitization at 950 °C for 10 min followed by air cooling and (b) electropulsing of air-cooled sample at 10.5 kA/mm ² [47].	15
Figure 1.11. Schematic diagram illustrating grain refinement (I) formation of γ -phase nuclei, (II) formation of γ -phase grains by the growth of nuclei, (III) α -phase nuclei formation during cooling and (IV) formation of α -phase grains by the growth nuclei [47].	16

Figure 1.12. The schematic diagram illustrates the thermal and athermal effects change in relation to the current density. [49].	18
Figure 1.13. schematic diagram explaining carbon movement and carbide precipitation [64].	22
Figure 1.14. Calculation of cementite formation rate from austenite at 360 °C [66]	23
Figure 1.15. TEM BF image showing nanostructured bainite and retained austenite in between [71]. (α_b is bainite and γ is austenite).	24
Figure 1.16. Schematic diagrams (a) showing different variants for a single (111) close packed plane of austenite and (b) hierarchy in a prior austenite grain showing arrangement of packets, blocks and laths [93].	27
Figure 1.17. Schematic diagram showing blocky retained austenite (BRA) and filmy retained austenite (FRA) in a prior austenite grain.	28
Figure 1.18. Rate of work hardening plot showing different stages of hardening in a low carbon bainitic steel [128].	34
Figure 1.19. Schematic illustration of the T_0 and T_0' curves . T is the temperature corresponding to the free energy curves [119].	36
Figure 1.20. Resistivity vs. temperature plot of different phases in steel [75].	38
Figure 1.21. SEM micrographs of the sample quenched after (a) heat treatment for 0.5 h at 750 °C, (b) electropulsing at a current density of 80 Amm ⁻² for 0.5 h [144].	40
Figure 1.22. TEM BF images of dual phase steel (a) before EP and (b) after EP. (α denotes ferrite, α' denotes martensite and θ is cementite) [145].	40
Figure 2.1. (a) Phase stability diagram calculated using Thermo-Calc and (b) TTT diagram of the D2 steel plotted using JMatPro software, austenitizing temperature of 970°and grain size of ASTM 6.	46
Figure 2.2. Schematic of (a) ECAP die with work pieces, (b) ECAPed work piece and (c) the cut-out plate from the ECAPed sample.	47
Figure 2.3. (a) Schematic diagram of casting and (b) elevation of cast plate.	48

- Figure 2.4.** Thermal cycles for hot-rolling, austenitization followed by air-cooling and austempering at 250°C. 49
- Figure 2.5.** (a) Schematic diagram of electropulsing set up and (b) Waveform of the electric pulse. 51
- Figure 2.6.** (a) Electropulsing set up, (b) sample holding position between electrodes and (c) schematic diagram of sample for electropulsing (arrow showing current flow direction), (i) clamping region (ii) area for microstructural characterization. 51
- Figure 2.7.** Schematic drawing of the tensile sample (all dimensions are in mm). 57
-
- Figure 3.1.** (a) Optical micrograph of D1 sample, (b) IQ map of ECAP-6 sample, (c) TEM BF image of ECAP-6 sample, image quality maps with superimposed grain boundaries of (d) D1 and (e) ECAP-6 samples, blue lines for high angle grain boundaries (misorientation angle > 15°) and red lines for low angle boundaries (2° < misorientation angle < 15°) and (f) SEM SE micrograph of ECAP-6 sample. [In figures b and d, the insets are enlarged view of the indicated area] 61
- Figure 3.2.** Waveform of Electropulsing 62
- Figure 3.3.** SEM SEI of (a) ECAP-6-EP-1 and (b) ECAP-6-EP-5, IQ maps of (c) ECAP-6-EP-1 and (d) ECAP-6-EP-5. 63
- Figure 3.4.** EBSD IQ maps superimposed with grain boundaries (a) ECAP-6-EP-1 and (b) ECAP-6-EP-5 samples and TEM BF images of (c) ECAP-6-EP-1 and (d) ECAP-6-EP-5 (arrow shows an equiaxed grain) samples. (Blue and red lines delineate HAGB and LAGB respectively). 64
- Figure 3.5.** EBSD grain intercept distributions (a) D1, (b) ECAP-6, (c) ECAP-6-EP-1 and (d) ECAP-6-EP-5. 65
- Figure 3.6.** Grain boundaries superimposed on EBSD KAM map in (a) ECAP-6 and its magnified region in (d), (b) ECAP-6-EP-1 and magnified region in (e) and (c) ECAP-6-EP-5 and magnified view in (f). 66
- Figure 3.7.** (a) XRD peaks of LCS-AR, ECAP-6, ECAP-6-EP-1 and ECAP-6-EP-5, (b) magnified view of (111) and (c) XRD peaks of ECAP-6-H1, and ECAP-6-H2. 67

Figure 3.8. (a) XRD peaks with magnified (110) of (a) D1, (b) ECAP-6, (c) ECAP-6-EP-1 (continue...)

69

Figure 3.9. Engineering stress vs. Engineering strain curves for ECAP-6 and ECAP-6-EP-1 samples.

72

Figure 4.1. Optical micrographs of (a) D2-25h, (b) D2-33h and (c) D2-48h and EBSD phase maps of (d) D2-25h, (e) D2-33h and (f) D2-48h. (α_b and RA stand for bainite, retained austenite respectively).

82

Figure 4.2. SEM secondary electron micrographs at higher magnifications of (a) D2-25h, (b) D2-33h, and (c) D2-48h, the corresponding histogram for apparent plate thickness of (d) D2-25h, (e) D2-33h and (f) D2-48h.

83

Figure 4.3. XRD patterns of (a) D2-25h, (b) D2-33h, (c) D2-48h, (d) (111) austenite peaks and (γ and α_b denotes austenite and bainite phases respectively)

85

Figure 4.4. KAM maps of retained austenite phase in (a) D2-25h, (b) D2-33h and (c) D2-48h and of bainite phase in (d) D2-25h, (e) D2-33h and (f) D2-48h samples.

87

Figure 4.5. TEM bright-field images of (a) D2-25h, (b) D2-33h, (c, e) D2-48h, (d) magnified view of bainite of D2-48h showing presence of carbides evidenced by the occurrence of Moire fringes and (f) selected area diffraction pattern corresponding to Fig.4.5e (ZA represents zone axis).

89

Figure 4.6. TEM micrographs of D2-48h (a) BF image (b) Dark field image, (c) corresponding diffraction pattern and (d) simulated pattern of γ [211] and α_b [011] zone axis.

90

Figure 4.7. TEM micrographs of D2-48h (a) BF image (b) corresponding diffraction pattern, (c), (d) and (e) are respective dark field images from spots 1, 2 and 3 of DP shown in Figure b.

90

Figure 4.8. Misorientation angle (MA) chart of (a) D2-25h, (b) D2-33h and (c) D2-48h, misorientation angles corresponding to K-S (blue lines) and N-W (red lines) OR are superimposed on phase map (the pink color is austenite and aqua color is bainite) of (d) D2-25h (e) D2-33h and (f) D2-48h.

91

Figure 4.9. EBSD IPF maps of normal direction of austempered samples of bainite phase (a) D2-25h, (b) D2-33h and (c) D2-48h, {001} pole figure maps showing orientation of austenite

(filled red circles) and bainite (open black circles) of (d) D2-25h (e) D2-33h and (f) D2-48h. (Corresponding K-S variant numbers are shown in respective positions). 93

Figure 4.10. T_0 and T_0' plots using MUCG 83 software. Black circle, red diamond and green square show carbon concentration at 250 °C in RA for D2-25h, D2-33h and D2-48h samples respectively. 96

Figure 4.11. Variant pairing with respect to V1 for (a) D2-25h (b) D2-33h and (c) D2-48h. 104

Figure 5.1. XRD patterns of (a) D2-25h (black colour) and D2-48h (red colour), (b) deconvolution of (111) austenite peaks of D2-25h sample and (c) (111) peak of D2-48h sample showing symmetric peak. 108

Figure 5.2. IPF maps along normal direction superimposed with high angle grain boundaries (black colour) (a) D2-25h, (d) D2-48h and GND density superimposed on IQ map in bainite phase (b) D2-25h, (e) D2-48h and in austenite phase (c) D2-25h and (f) D2-48h (misorientation angle of 15°-65° is referred as high angle grain boundaries). 110

Figure 5.3. TEM bright-field images of (a) D2-25h and (b) D2-48h samples. 111

Figure 5.4. Engineering stress (MPa) vs. strain (%) plots of D2-25h (black) and D2-48h (red) samples. 112

Figure 5.5. True plastic stress- true plastic strain plots, (a) D2-25h (b) D2-48h fitted with different work hardening equations. 113

Figure 5.6. (a) Logarithm work hardening rate vs. logarithm (pre-strain+true plastic strain) plots showing different stages of work hardening and (b) true stress vs true strain plots of D2-25h (black) and D2-48h (red) samples displaying work hardening stages. 114

Figure 5.7. XRD patterns of tensile tested samples. 118

Figure 5.8. A schematic showing microstructural changes after stage II of work hardening in (a) D2-25h and (b) D2-48h samples (The light blue regions represent low carbon concentration, while the deep blue regions represent high carbon concentration). 120

Figure 6.1. (a) Wave form of electropulsing of D2-48h sample, (b) Realtime image of the sample during electropulsing treatment and (c) Colour of the steel at different temperatures (°C) [230]. 123

Figure 6.2. SEM secondary electron micrographs of (a) D2-48h, (b) D2-48h-EP-1, and EBSD phase maps of (c) D2-48h, (d) D2-48h-EP-1 (Symbol α_b denotes bainite and RA is retained austenite, and FRA is filmy retained austenite). 125

Figure 6.3. XRD patterns of (a) D2-48h, D2-48h-EP-1, D2-48h-EP-5, D2-48h-EP-1-LCD and (b) magnified view of (111) and (110) peaks of austenite and bainite phases respectively. 126

Figure 6.4. TEM BF images of (a) D2-48h with a magnified region of bainite showing carbides, (b, c) D2-48h-EP-1 and (d) DF images of D2-48h-EP-1 sample. A blocky retained austenite region of D2-48h-EP-1 sample is shown in (e) and its corresponding DP in (f). 129

Figure 6.5. TEM images of a BRA region of D2-48h-EP-1 sample (a) BF image and corresponding DP, DF from DP (b) spot 1 and (c) spot 3. (d) BF image showing FRA and its magnified region and corresponding DP in (e) and (f) respectively. (The spot size of beam is narrowed to 3 nm). 129

Figure 6.6. TEM micrographs of D2-48h-EP-5 (a) BF (b) DP, (c) DF and (d) BF image showing martensite formation in BRA. 130

Figure 6.7. TEM images of D2-48h-EP-1-LCD sample (a) BF, (b) DP and (c) DF from spot shown in DP in Figure b. (d) simulated diffraction pattern corresponding to α_b [113] zone axis. 131

Figure 6.8. TEM micrographs of D2-48h-EP-1-LCD from a BRA region (a) BF, (b) BF (magnified region of circled area in figure a), (c) DP, (d) DF1 and (e) DF2. (f) simulated diffraction pattern corresponding to α_m [113] zone axis. 132

Figure 6.9. KAM maps of bainite (a) D2-48h, (b) D2-48h-EP-1 and of retained austenite (c) D2-48h (d) D2-48h-EP-1. 133

Figure 6.10. Variant pairing with respect to V1 for (a) D2-48h (b) D2-48h-EP-1, (c) D2-48h-EP-5 and (d) D2-48h-EP-1-LCD. 135

Figure 6.11. Applied force vs. indentation depth plot 136

Figure 6.12. (a) Stability of phases as a function of temperature and (b) Mean radius of cementite calculated using TC-PRISMA. 138

Figure 7.1. Micrographs of D2-A sample (a) Optical, (b) SEM-SE, (c) IQ map and (d) phase map. (α_m and RA denote martensite and retained austenite respectively) 148

Figure 7.2. Optical micrographs of (a) D2-A-EP-1, (b) D2-A-EP-1-LCD and SEM-SE images of (c) D2-A-EP-1, (d) D2-A-EP-1-LCD samples. 149

Figure 7.3. EBSD-IQ maps of (a) D2-A-EP-1, (b) D2-A-EP-1-LCD and phase maps of (c) D2-A-EP-1, (d) D2-A-EP-1-LCD samples. 150

Figure 7.4. Grain boundaries are superimposed in IQ maps of bainite (a) D2-A, (b) D2-A-EP-1 and (c) D2-A-EP-1-LCD and retained austenite (d) D2-A, (e) D2-A-EP-1 and D2-A-EP-1-LCD. 151

Figure 7.5. KAM map of martensite phase (a) D2-A, (b) D2-A-EP-1 and (c) D2-A-EP-1-LCD and austenite phase (d) D2-A, (e) D2-A-EP-1 and (f) D2-A-EP-1-LCD samples. 152

Figure 7.6. XRD peaks of (a) D2-A, (b) D2-A-EP-1, (c) D2-A-EP-1-LCD and (d) D2-M samples. 153

Figure 7.7. TEM images of D2-A sample (a) BF and corresponding DP, (b) BF image showing midrib in a lenticular martensite, (c) magnified BF region, (d) corresponding DP, (e and f) DF taken from indicated regions of DP in Figure d showing midrib and carbides in matrix phase respectively. 155

Figure 7.8. TEM images of D2-A-EP-1 sample (a) BF, (b) DF (c) BF image of RA and (d) SAEDP corresponding to position circled in the BF image of Figure c. 156

Figure 7.9. TEM images of D2-A-EP-1-LCD sample (a-c) BF, (d) DP corresponding to Figure c (e, f) DF images corresponding position 1 and 2 in the DP of Figure 7.9d. 157

Figure 7.10. Applied force vs. indentation depth plot 158

List of Tables

	Page No.
Table 1.1. Mechanical properties of samples, with and without electropulsing [47].	16
Table 1.2. Bainite-austenite OR with ideal misorientation angle [92].	26
Table 1.3. Twenty-four variants of the K–S OR and corresponding CP and Bain groups [90].	27
Table 2.1. Chemical composition of the two selected materials (mass %).	46
Table 2.2. Details of EP parameters	52
Table 3.1. Details of crystallite size, lattice strain, and dislocation density	71
Table 3.2. Tensile and hardness testing results	72
Table 4.1. Estimated lattice parameter, carbon content, volume fraction obtained by Rietveld refinement.	85
Table 4.2. XRD line profile analysis results for crystallite size, micro-strain, and dislocation density.	86
Table 4.3. Calculated and measured bainite plate thickness data.	101
Table 5.1. Tensile properties and hardness of the steels after selected austempering treatments.	112
Table 5.2. Fitting parameters of the Swift model	113
Table 6.1. XRD peak profile analysis	127
Table 6.2. Results of instrumented hardness testing	136

Table 6.3. Diffusion coefficient and length of atomic movement.	138
Table 7.1. XRD peak profile analysis	154
Table 7.2. Results of instrumented hardness testing	158

List of Symbols

γ	Shear strain
φ	Angle of internal channel
ψ	Outer arc of curvature
N	Number of passes
ε_N	Equivalent strain after N passes
ε_{vM}	Equivalent von Mises strain
σ_y	Yield stress
σ_i	Friction stress
K_y	Strength coefficient
d	Grain size
γ	Austenite
$V_{\gamma f}$	Volume fraction of filmy retained austenite
$V_{\gamma b}$	Volume fraction of blocky retained austenite
V_{ab}	Volume fraction of bainite
σ_{Fe}	Frictional strength of pure iron
σ_{SS}	Solid solution strengthening from substitutional elements
σ_c	Strengthening contribution due to carbon
t_b	Thickness of bainite plate
ρ	Dislocation density
\bar{x}	Alloy average carbon concentration
x_b	Carbon concentration of the bainitic ferrite
W_f	Work done during passage of electric current
μ	Magnetic susceptibility
I	Current density
V	Volume of nucleus
σ_2	Electrical conductivities of nucleating phases
I_e	Nucleation rate in a current carrying system
I_0	Nucleation rate of the current-free system
D	Diffusivity
λ	Atomic jump distance
ΔW_0	Gibbs energy change in the current-free material
ΔW_f	Gibbs energy change in the current carrying system
K	Boltzmann constant
T	Temperature
J	Total diffusion flux
J_e	Diffusion flux due to current
D_0	Pre-exponential diffusion factor
C_i	Vacancy concentration
Z^*	Effective charge
e	Charge of electron
R_{wp}	R-weighted pattern
$y_i (obs)$	Observed intensity
$y_i (calc)$	Calculated intensity
w_i	Weight factor
χ^2	Goodness of fit

S	Scherrer constant
B	Crystallite size
ΔK_c	Broadening of a XRD peak
a_γ	Lattice parameter of austenite
w_c	Mass % of carbon
w_{Mn}	Mass % of Manganese
w_{Al}	Mass % of Aluminum
w_{Cr}	Mass % of chromium
w_{Ni}	Mass % of nickel
w_{Si}	Mass % of Si
a_α	Lattice parameter of bainite
ΔK	Peak width
K_d	Diffraction vector
M	Dislocation screening parameter
\bar{C}	Dislocation contrast factor
σ	True stress
ε	True strain
σ_0	Pre-stress
ε_0	Pre-strain
σ_s	Saturation stress
σ_{it}	True yield stress
ΔT	Temperature rise
Δt	Pulse period
C_p	Heat capacity
d	Density
τ_{ew}	Resolved shear stress
f_{ew}	Electron wind force
K_{ew}	Electron force coefficient
b	Burgers vector
M_d	Mobility of dislocations
N_a	Density of atoms
δ	Skin depth
f	Frequency
μ_m	Permeability
σ_{RT}^Y	Yield strength of the austenite at room temperature
σ_{IT}^Y	Yield strength of the austenite at the isothermal temperature
d'	Average austenite grain size
σ_{dis}^Y	Yield strength due to dislocation density in austenite
M_t	Taylor factor
μ	Shear modulus
L	Diffusion distance
Q	Activation energy
R	Universal gas constant

Abbreviations

ECAP	Equal-Channel Angular Pressing
XRD	X-Ray Diffraction Technique
TEM	Transmission Electron Microscopy
EBSD	Electron Back-Scattered Diffraction
UFG	Ultra Fine-Grained
RA	Retained Austenite
CW	Cold Working
BF	Bright Field
SEM	Scanning Electron Microscopy
BRA	Blocky Retained Austenite
FRA	Filmy Retained Austenite
EP	Electropulsing
TTT	Time-Temperature-Transformation
ASTM	American Society for Testing And Materials
SEI	Secondary Electron Imaging
IQ	Image Quality
HAGB	High Angle Grain Boundaries
LAGB	Low Angle Grain Boundaries
KAM	Kernel Average Misorientation
LCS	Low Carbon Steel
AR	As Received
DP	Diffraction Pattern
OR	Orientation Relationship
IPF	Inverse Pole Figure
GND	Geometrically Necessary Dislocations
LCD	Low Current Density
DF	Dark Field
SE	Secondary Electron
CP	Close Packed
SPD	Severe Plastic Deformation

NSM	Nanostructured Materials
SV	Surface To Volume Ratio
GNB	Geometrically Necessary Boundaries
UTS	Ultimate Tensile Strength
YS	Yield Strength
EPT	Electropulsing Technique
HV	Vickers Hardness
TRIP	Transformation Induced Plasticity
AC	Air Cooling
CCPS	Capacitor Charging Power Supply
CRO	Cathode Ray Oscilloscope
FEG	Field Emission Gun
ICDD	International Centre for Diffraction Data
PDF	Powder Diffraction File
GOF	Goodness Of Fit
WH	Williamson-Hall
MWH	Modified-Williamson-Hall
OIM	Orientation Imaging Microscopy
UE	Uniform Elongation
TE	Total Elongation
FCC	Face Centered Cubic
FWHM	Full Width at Half Maxima
BCC	Body Centered Cubic
NW	Nishiyama Wasserman
SIM	Strain Induced Martensite
WQ	Water Quenched